

Resonant X-ray Sum-Frequency-Generation Spectroscopy of K-Edges in Acetyl Fluoride

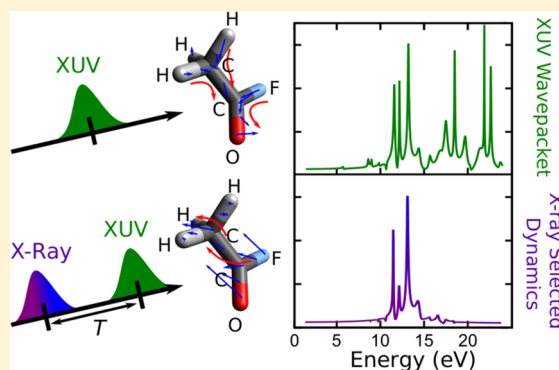
Adam Bruner,^{*,†} Stefano M. Cavaletto,^{*,†} Niranjana Govind,^{*,‡} and Shaul Mukamel^{*,†}

[†]Department of Chemistry and Physics and Astronomy, University of California, Irvine, California 92697, United States

[‡]Environmental Molecular Sciences Laboratory, Pacific Northwest National Laboratory, Richland, Washington 99352, United States

S Supporting Information

ABSTRACT: Resonant X-ray sum-frequency generation is calculated for excitations of the fluorine and the oxygen core K-edge in acetyl fluoride using real-time time-dependent density functional theory. The signal is generated by an extreme-ultraviolet pulse followed by an X-ray pulse with variable delay T . The X-ray pulse is tuned to different element-specific core excitations and used to probe the dynamics of a valence electronic wave packet. A two-dimensional signal is recorded depending on the dispersed X-ray pulse frequency and the frequency conjugated to T , revealing the couplings between core and valence excited states. Molecular orbital decomposition of the signal reveals which regions of the molecule contribute to the X-ray excitation.



1. INTRODUCTION

X-ray absorption spectroscopy has long been used to study core electrons and their involvement in molecular electronic structure. Core electrons are highly localized around the corresponding atoms in a molecule, with element-specific excitation energies lying in the soft- to hard-X-ray regime. By resonantly exciting core electrons, it is thus possible to monitor a desired region of a molecule with high spatial selectivity. However, core excitations are often limited by their lifetime, which restricts the observation window of the dynamics of the associated absorption spectra and satellite peaks.

With the advent of ultrashort, coherent X-ray pulses from high-order harmonic generation (HHG)^{1–3} and X-ray free-electron lasers (XFELs),^{4–8} it is now possible to directly access core excited states in ultrafast time scales via time-resolved X-ray spectroscopies. Multidimensional nonlinear spectroscopies, developed during the past decades in the infrared and visible range to monitor vibrational and electronic coherences in molecules,^{9,10} can be extended to the X-ray regime and probe valence and core electronic dynamics with a broader bandwidth.^{11,12}

Sum-frequency generation (SFG) is a second-order nonlinear wave-mixing process, which is routinely used by combining infrared and visible pulses to probe molecular vibrations.¹³ Optical/X-ray analogues were proposed^{14,15} but only very recently demonstrated thanks to the unprecedented brightness offered by XFELs.¹⁶ Time-resolved ultraviolet/X-ray sum-frequency diffraction has been put forward to image ultrafast electron dynamics.^{17,18} First, the ultraviolet pump generates a valence electronic wave packet consisting of a superposition of several states. The subsequent dynamics are then imaged via the off-resonant diffraction of a broadband X-

ray pulse at different delays. A related all-X-ray setup has also been proposed to probe the dynamics of a core electronic wave packet generated by an initial X-ray pulse.¹⁹ This off-resonant X-ray SFG setup offers time- and space-resolved snapshots of the evolution of transient charge densities. In addition, studies of X-ray diffraction²⁰ have shown that the resonant scattering signal contains information on time-resolved current densities²¹ in molecules and crystals.^{22,23}

In this paper, we calculate resonant X-ray sum-frequency-generation (XSF) signals (see diagrams in Figure 1) to time resolve the dynamics of a valence electronic wave packet initiated by an extreme-ultraviolet (XUV) pulse. Combined optical/X-ray wave-mixing $\chi^{(3)}$ experiments have already been demonstrated,¹⁶ which renders XSF—the simpler lower-order $\chi^{(2)}$ nonlinear signal—also feasible. In contrast to off-resonant XSF, here, the delayed X-ray probe is tuned to an element-specific core excitation, enabling the post selection of different states in the valence-initiated wave packet. By tuning the X-ray pulse to different core excited states, this also enables one to gain information about the properties of the molecular orbitals contributing to the valence electronic wave packet.

Simulations are performed for the oxygen and fluorine K-edges in acetyl fluoride. With these two soft-X-ray core transitions spectrally well separated by more than 150 eV, the molecule can provide a suitable benchmark for nonlinear XSF, revealing how different nearby cores can select and couple to specific valence dynamics. The small size of the molecule also simplifies the numerical simulation of its dynamics when driven by XUV and X-ray pulses. Thanks to

Received: June 27, 2019

Published: November 12, 2019

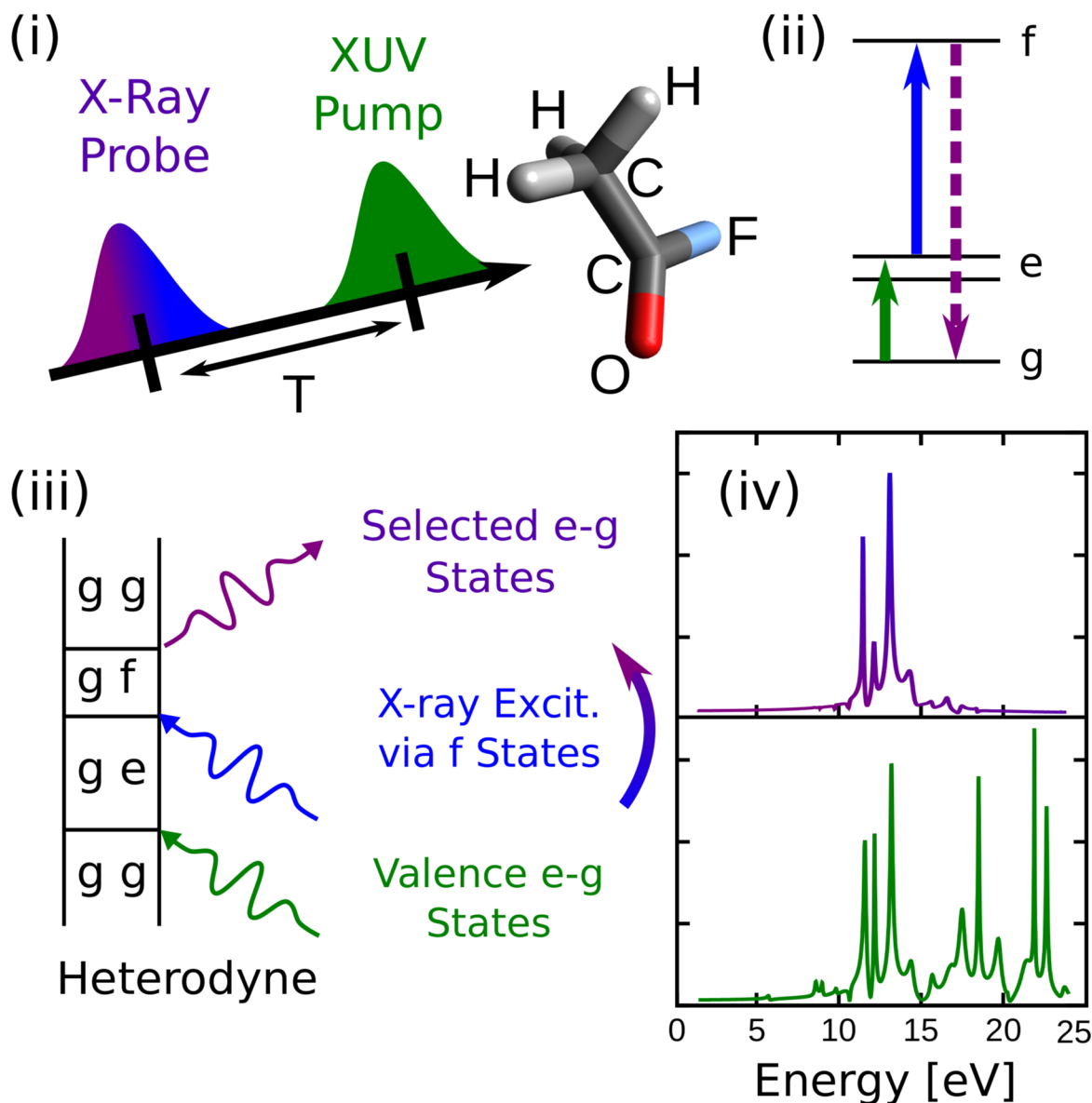


Figure 1. (i) Resonant XSFG pulse sequence and optimized geometry of the acetyl fluoride molecule. (ii) Relevant level scheme. The letters g , e , and f denote the ground and valence excited and core excited states, respectively. (iii) Ladder diagram for the signal. (iv) Comparison of the XSFG signal resonant to the oxygen K-edge (top) and the XUV linear absorption from the real-time time-dependent dipole of the e - g wave packet (bottom) illustrates that different valence states contribute in the two techniques.

the element-specific core transitions, resonant XSFG should allow one to follow how the fluorine or oxygen electrons influence differently reactions at the carbonyl carbon in acetyl fluoride.

2. METHODS

We begin with an overview of real-time current density and resonant XSFG. This includes a brief review of the minimal-coupling Hamiltonian, followed by the vector potentials relevant to this multidimensional technique and a presentation of the resonant XSFG signal. We then provide the simulation details to obtain the time-dependent resonant XSFG signal via a two-step protocol with RT-TDDFT.

Real-Time Current Density and Resonant XSFG. The XSFG setup is sketched in Figure 1i. This stimulated heterodyne signal involves three interactions with the field. The first interaction with an XUV pulse creates a valence

electronic wave packet, giving rise to coherences between the ground state g and a superposition of valence excited states e . A subsequent broadband X-ray probe is responsible for the two following interactions marked by the blue and purple lines in Figure 1ii and iii, which represent a stimulated Raman process via the core excited state f .

The signal is derived by using the minimal-coupling interaction Hamiltonian, which, for resonant excitations, is given by

$$\hat{H}_{\text{int}}(t) = - \int d^3r \hat{j}(\mathbf{r}) \cdot \mathbf{A}(\mathbf{r}, t) \quad (1)$$

with the current-density operator of the material $\hat{j}(\mathbf{r})$ and the time-dependent vector potential $\mathbf{A}(\mathbf{r}, t) = \mathbf{A}_{\text{XUV}}(\mathbf{r}, t + T) + \mathbf{A}_{\text{X}}(\mathbf{r}, t) + \text{c.c.}$ Here, the XUV vector potential $\mathbf{A}_{\text{XUV}}(\mathbf{r}, t + T) = \mathbf{A}_{\text{XUV}}(t + T)e^{ik_{\text{XUV}} \cdot \mathbf{r}}$ is centered at $t = -T$, and the X-ray pulse vector potential $\mathbf{A}_{\text{X}}(\mathbf{r}, t) = \mathbf{A}_{\text{X}}(t)e^{ik_{\text{X}} \cdot \mathbf{r}}$ is centered at $t = 0$, with

wave vectors k_{XUV} and k_X , respectively. For resonant excitations, contributions to the minimal-coupling interaction Hamiltonian involving the charge density can be neglected.

We have calculated the frequency-dispersed XSGF signal due to X-ray photon emission from f to g . The spontaneous homodyne signal generated when the emitted photon is not overlaid with an external classical field is quadratic in the current density.^{9,17} In our case, however, with a broadband X-ray pulse, the photons are emitted into modes which are already occupied by $A_X(r, t)$, resulting in heterodyne detection. A formal definition of the stimulated XSGF signal, in terms of the rate of change of the number of photons occupying a given mode of frequency Ω_2 , is provided in the [Supporting Information](#). The signal is related to the Fourier transform of the expectation value of the current density

$$S(\Omega_2, T) \propto -2\text{Im} \int d^3r \int dt \int dt' A_X^*(r, t) \cdot \langle \hat{j}(r, t') \rangle e^{-i\Omega_2(t-t')} \quad (2)$$

which depends on the interpulse delay T via the evolution of $\langle \hat{j}(r, t') \rangle$. The stimulated heterodyne signal is linear in the current density, which simplifies its interpretation compared to homodyne detection.

We shall display the 2D spectrum of the resonant stimulated XSGF signal

$$\tilde{S}(\Omega_1, \Omega_2) = \left| \int S(\Omega_2, T) e^{i\Omega_1 T} dT \right| \quad (3)$$

by scanning the delay between the pump and probe pulses, where the second and third interactions are resonant with either the fluorine K-edge or the oxygen K-edge in acetyl fluoride.

For sufficiently weak pulses, the contribution of the three interactions in [Figure 1](#) ii and iii to the XSGF signal can be described via a perturbative expansion of $\langle j^{(2)}(r, t) \rangle$ to second order in the interaction Hamiltonian of [eq 1](#). In such a case, [eq 2](#) can be written as

$$S(\Omega_2, T) \propto 2\text{Im} \int dt \int dt' \int_0^\infty dt_1 \int_0^\infty dt_2 \sum_{e,f} e^{-i\Omega_2 t} A_X^*(t) \cdot j_{gf}(-k_X, t_1 + t_2) e^{i\Omega_2 t'} A_X(t' - t_2) \cdot j_{fe}(k_X, t_1) A_{XUV}(t' + T - t_1 - t_2) \cdot j_{eg}(k_{XUV}, 0) \quad (4)$$

with the expectation values of the current-density operators in the interaction picture

$$j_{ab}(\mathbf{k}, t) = \int d^3r e^{i\mathbf{k}\cdot\mathbf{r}} \langle a | e^{i\hat{H}_0/\hbar t} \hat{j}(\mathbf{r}) e^{-i\hat{H}_0/\hbar t} | b \rangle \quad (5)$$

and the Hamiltonian of the molecule \hat{H}_0 . Although the signals presented in this work are not calculated by the perturbative expansion (see [Simulation Details](#)), [eq 4](#) provides insight and a detailed description of the pathways contributing to the real-time signal in [eq 2](#).

Simulation Details. The XSGF signal ([eq 2](#)) was calculated using time-dependent density functional theory (TDDFT),^{24–28} which offers a favorable trade-off between speed and accuracy. Both linear-response (LR) and real-time (RT) TDDFT simulations have been used to describe core ionization dynamics,²⁹ near and above ionization electronic excitations,³⁰ strong-field ionization,^{31–34} ultrafast charge

migration,³⁵ charge transfer,^{36–44} excited state absorption,^{45–47} optical rotation,⁴⁸ X-ray absorption,^{49–53} and much more.

TDDFT calculations often employ the adiabatic approximation, where the exchange-correlation potential only depends on the density at a given instant in time instead of the entire history, i.e., memory effects are neglected.⁵⁴ Although this is sufficiently accurate to describe single excitations, doubly excited states (our states f) are not accounted for.^{55,56} However, the two-step calculations employed here can describe double excitations and excited-state dynamics.^{29,45,57}

Optical Pump, Resonant X-ray Couplings

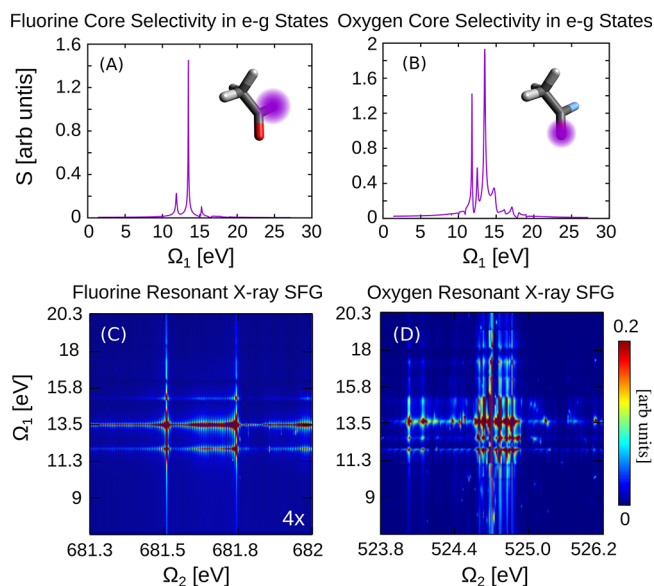


Figure 2. Equation 3 integrated over Ω_2 showing $|g\rangle\langle e|$ dynamics selected through f core states (top row). 2D spectra of the XSGF signal, [eq 3](#), show the valence-core coupling (bottom row). The $|g\rangle\langle e|$ dynamics that are selected by resonant X-ray core excitation are observed in the Ω_1 axis of the 2D SFG signal at the resonant frequency of the core (Ω_2). Resonant excitation through the K-edges of fluorine (left) and oxygen (right) offers additional selectivity of $|g\rangle\langle e|$ dynamics.

The ground state geometry of the acetyl fluoride molecule ([Figure 1](#) i) was optimized using the B3LYP^{58,59} exchange-correlation functional and aug-cc-pVTZ basis set⁶⁰ with DFT. DFT offers an excellent balance of speed and accuracy compared to other electronic-structure methods. This speed-up is especially useful here for describing the many states (valence to core) and is important when simulating larger systems, where higher-level calculations are not tractable. The B3LYP functional was selected because hybrid functionals offer a good balance of electron correlation and exchange, which is necessary for core excitations.²⁹ The large basis set ensures a good convergence of the ground state. The molecule has been oriented such that z-polarized light has excitation contributions both along and perpendicular to the molecular axis ([Supporting Information](#)). RT-TDDFT open-shell calculations were performed at the B3LYP/6-31G⁶¹ level with a 0.05 au time step to avoid aliasing and to capture the ultrafast dynamics associated with the core excitation. Also, the choice of basis for the RT calculations offers a good balance between the charge migration description and the computational speed.

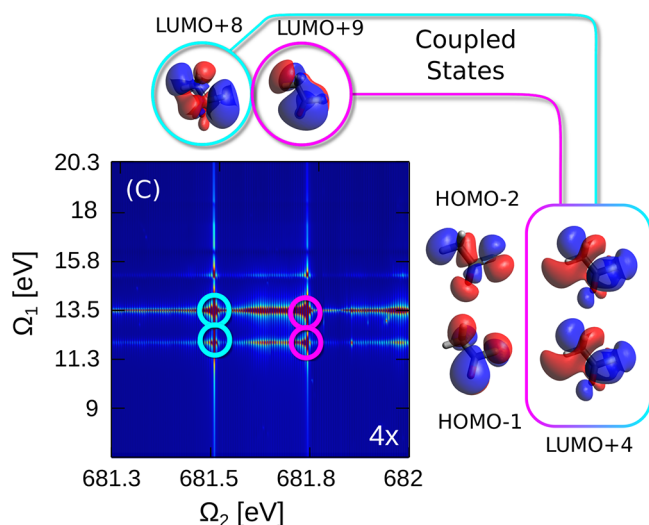


Figure 3. Fluorine core–valence couplings in 2D X-ray sum-frequency generation (XSF) spectra using eq 3. The same units are used as in Figure 2. The fluorine core to unoccupied excitations (top, x -axis) are coupled to the valence to unoccupied excitations (right, y -axis). At 681.5 eV, the K-edge excitation to L+8 shares a high degree of overlap with valence transitions from H–1 \rightarrow L+4 and H–2 \rightarrow L+4, thereby selecting two dynamics involving the L+4 (teal couplings) in the XSF. Similarly, the core excitation at 681.7 eV to L+9 couples strongly to the same two valence excitations (pink couplings).

The two-step protocol was performed using the RT-TDDFT module⁶² implemented in the development version of NWChem⁶³ to compute the time-evolving density matrix below. In the first step, the molecule is excited by the XUV pulse to determine the orbital occupations of the excited state DFT reduced single-electron density matrix. A second RT-TDDFT calculation is then performed where these occupations are used to describe the initial ($t = 0$) singly excited reduced density matrix.²⁹ This density matrix is expanded in the valence basis set to obtain a nonstationary state (wave packet), which evolves in time from the initial condition. During its time evolution, the system is excited by the X-ray probe field to a doubly excited state. The ground state $|g\rangle$ is thus built from the ground state Kohn–Sham orbitals, while the excited states $|e\rangle$ are an expansion in the first-excited-state basis, and $|f\rangle$ are second excitations beyond that excited state.

The two-step protocol in RT-TDDFT has been used to obtain the time- and space-dependent currents $\langle \hat{j}(r, t) \rangle$ for the calculation of the spectrum via eqs 2 and 3. In step 1 of the protocol, we used a z -polarized Gaussian pump centered at 13.5 eV with a 32 as pulse. Since the pump interacts only once with the molecules, we were careful to ensure that the density matrix in our calculations is prepared in a $|g\rangle\langle e|$ coherence state, i.e., our current is first order in A_{XUV} and less than 1% of an electron is populated in the excited state. The dynamics for each real-time simulation are obtained by solving the TDDFT equations of motion^{24,64}

$$i \frac{\partial \rho(t)}{\partial t} = [\mathbf{F}(t), \rho(t)] \quad (6)$$

where the time-dependent Fock matrix $\mathbf{F}(t)$ is given by

$$\begin{aligned} \mathbf{F}[\rho(t)] = & \mathbf{H}^{\text{core}} + \mathbf{G}^J[\rho(t)] + \alpha \mathbf{G}^K[\rho(t)] \\ & + \beta \mathbf{G}^{\text{X-DFT}}[\rho(t)] + \gamma \mathbf{G}^{\text{C-DFT}}[\rho(t)] \\ & - \int d^3r \left(\vec{j}(r) - \frac{1}{2} \rho(r) \vec{A}(r) \right) \cdot \vec{A}(r) \end{aligned} \quad (7)$$

The bold symbols here denote matrices written in the single-electron state basis $\{\phi_\mu(r)\}$. The core-Hamiltonian \mathbf{H}^{core} is the sum of the nuclear repulsion energy and the one-electron energy, $\mathbf{G}^J[\rho(t)]$ is the Coulomb electron repulsion. α , β , and γ are the coefficients for the Hartree–Fock exact exchange $\mathbf{G}^K[\rho(t)]$, the DFT exchange $\mathbf{G}^{\text{X-DFT}}[\rho(t)]$, and the DFT correlation $\mathbf{G}^{\text{C-DFT}}[\rho(t)]$, respectively, for a hybrid DFT functional. The last term represents the minimal-coupling interaction Hamiltonian with the external vector potential $\vec{A}(r)$, where $\vec{j}(r)$ is the current density and $\rho(r)$ is the charge density. For resonant interactions, the A^2 term is small and is neglected in our calculations.

The dominant state occupations for the excited-state density matrix $\mathbf{P}(t)$ are used to define the orbital populations needed for step 2 of our protocol. The excited-state density matrix is expanded in the state basis to produce the nonstationary g – e wave packet. RT-TDDFT is then used for step 2, where the time-propagated wave packet is probed by the X-ray pulse. In both steps, the vector components of the current-density matrix \mathbf{j} were obtained by

$$\vec{j}(t) = \mathbf{P}(t) \vec{v} \quad (8)$$

where \vec{v} is the associated charge velocity. The expectation value of the current density in space and time can then be obtained from the matrix elements $\hat{j}_{\mu\nu}(t)$ of the current density matrix (eq 8) via the explicit space dependence of the basis states $\phi_\mu(r)$

$$\langle \hat{j}(r, t) \rangle = \sum_{\mu\nu} \hat{j}_{\mu\nu}(t) \phi_\mu(r) \phi_\nu^*(r) \quad (9)$$

These time-dependent current densities obtained through RT-TDDFT are then inserted into eqs 2 and 3 for the calculation of the XSF signal.

By tuning the X-ray pulse in the second simulation to the oxygen K-edge or the fluorine K-edge, the molecule is excited to the f core excited state, thereby selecting desired dynamics from the g – e valence excited states. The selectivity gained by the resonant probe is displayed in Figure 1iv and further discussed below.

3. RESULTS

Core Selectivity. The 2D XSF spectrum was calculated for both the fluorine and the oxygen K-edges in acetyl fluoride. The fluorine core was excited by a broadband Gaussian X-ray probe centered at 685 eV of 320 as. In a separate calculation, the oxygen core was excited by interaction with a similar X-ray probe centered at 534 eV. The 2D XSF spectra (eq 3) were then computed by varying the delay T between pump and probe pulses. The central frequencies of the pulses have been slightly shifted from the TDDFT K-edge energies (see Figures 3 and 4) to cover a broad range of core states. All line widths are generated by damping the time signal at $\tau = 150$ au to accelerate convergence of the Fourier transform.

Figure 2 (top row) shows the valence states in the g – e coherence that are selectively excited through the core during the X-ray probe and is obtained by integrating eq 3 over Ω_2 . By

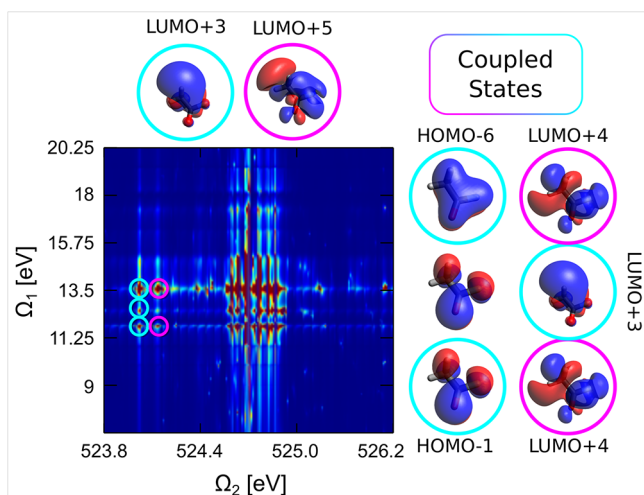


Figure 4. Oxygen core–valence couplings in 2D X-ray sum-frequency generation (XSFG) spectra obtained from eq 3. The same units are used as in Figure 2. The oxygen core to unoccupied excitations (top, x -axis) are coupled to the valence to unoccupied excitations (right, y -axis). At 523.9 eV, the O K-edge excitation to L+3 shares a high degree of overlap with orbitals in valence transitions from H-1 \rightarrow L+4 and H-6 \rightarrow L+4, which select the valence dynamics at 11.8 eV and 13.5 eV, respectively. The O core excitation includes the L+3 state, which also strongly contributes to the valence excitation at 12.5 eV, thereby selecting these additional state dynamics via the core. The O core excitation at 524.2 eV to L+5 has limited overlap with the states contributing to valence dynamics at 12.5 eV, and only selects those from H-6 \rightarrow L+4 and H-1 \rightarrow L+4.

scanning T , we capture the time evolution of the surviving valence states in the X-ray core absorption spectra. The 2D spectra (Figure 2, bottom row) reveal which valence states couple to the core, and are thereby selected in the probe interaction. By comparing the spectra for fluorine (left) and oxygen (right), we see that different states are selected by each core.

To determine the states selected by the core excitation, we examined the dominant molecular orbital pair contributions^{51,65–67} to each coupled state in the 2D XSFG spectra. In Figure 3, the dominant states excited by the fluorine core are shown along the top (x -axis), the first at 681.5 eV and another at 681.7 eV. On the right (y -axis), the dominant states contributing to the valence excitations are shown. States that have high overlap (scalar product) and symmetry are strongly coupled. We see that the core excitation to the LUMO+8 at 681.5 eV is coupled to the LUMO+4 both at 11.8 eV (H-1 \rightarrow L+4) and at 13.4 eV (H-2 \rightarrow L+4). In addition, we see that the second core excitation to the LUMO+9 at 681.7 eV is also coupled to the same two valence excitations. We note that all of these states are localized around the fluorine atom, demonstrating the spatial selectivity due to the localization of the core state.

Similarly, the dominant states selected by the oxygen core excitation and obtained from the 2D XSFG spectra are displayed in Figure 4 (top, x -axis). Like the fluorine core excitation (Figure 3), there are strong valence couplings at 11.8 eV (H-1 \rightarrow L+4) and 13.5 eV (H-6 \rightarrow L+4), as shown on the right y -axis. In oxygen, however, we also note an additional set of couplings to the valence state at 12.5 eV. The first core excitation at 523.9 eV involves the LUMO+3, which also contributes strongly to the valence dynamics at 12.5 eV.

The large cluster of bands near 525 eV continues the trend of couplings at higher energies, e.g., L+5, L+8, and L+9, with higher σ character as we move away from the excitation edge. The states in this band, however, are composed of many of such orbitals, so that the corresponding couplings may not be assigned to one or two orbitals. It should be noted that the states selected by the oxygen core excitation largely cover the space around the oxygen atom, again offering spatial selectivity based upon the localization of the core state.

These results can also be interpreted in terms of the nonlocal current density obtained in our simulations. Figure 5

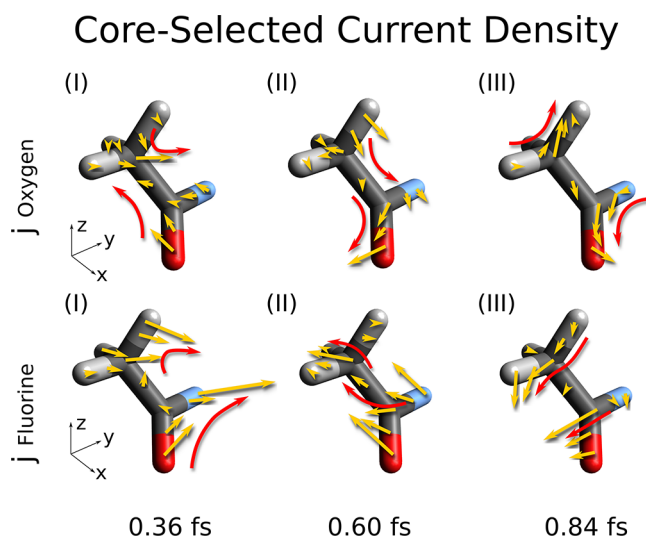


Figure 5. Time-dependent current densities (eq 9) corresponding to the oxygen (top) and fluorine (bottom) K-edge excitations. Each snapshot shows the instantaneous current-density vectors (yellow) at different times following the X-ray probe pulse. The red vectors represent the longest continuous paths of tip to tail vectors. Note that the current density for the oxygen core excitation has longer vectors near the oxygen, with less current on the fluorine atom. In contrast, the fluorine core-excited dynamics show increased current near the fluorine atom. Exciting specific cores offers selectivity of different dynamics and the relevant molecular regions.

shows snapshots of the time-dependent current-density vectors of the dynamics obtained by eq 9 with the probe interaction. The oxygen core-excited dynamics (top) show large currents near the oxygen atom, while the fluorine core excitations (bottom) show increased currents near the fluorine atom. The vectors from both cores have not been scaled and are directly comparable to each other. By excitation of different cores, we gain selectivity of different dynamics as well as molecular regions. This allows visualization of the currents for the core-selected dynamics.

4. CONCLUSIONS

Resonant XSFG can select, track, and interpret the time-evolution of excited-state dynamics such as charge migration. Core excitation can select valence states via different core excited states. In the nonlocal description of the current, the minimal-coupling interaction Hamiltonian goes beyond the dipole approximation. Our resonant XSFG spectrum is based on a nonlocal description of the light–matter interaction and allows us to capture each resonant interaction with the field. In addition, the Fourier transform over the delay between pulses allows us to determine which valence states are selected

through the core excitation. We find that the excitations through oxygen and fluorine cores select different valence states. These states can then be analyzed using molecular orbital decomposition to determine which states are coupled and how they are localized in the molecule. Resonant XSFSG offers a powerful way to select and interpret the states excited through the core, as well as the affected regions in the molecule.

■ ASSOCIATED CONTENT

Supporting Information

The Supporting Information is available free of charge at <https://pubs.acs.org/doi/10.1021/acs.jctc.9b00642>.

Coordinates of the acetyl fluoride molecule and a derivation of the resonant stimulated XSFSG signal (PDF)

■ AUTHOR INFORMATION

Corresponding Authors

*E-mail: abrunner@uci.edu.

*E-mail: scavalet@uci.edu.

*E-mail: niri.govind@pnnl.gov.

*E-mail: smukamel@uci.edu.

ORCID

Adam Bruner: 0000-0002-0705-1690

Stefano M. Cavaletto: 0000-0003-1516-7519

Niranjan Govind: 0000-0003-3625-366X

Shaul Mukamel: 0000-0002-6015-3135

Notes

The authors declare no competing financial interest.

■ ACKNOWLEDGMENTS

The support of the Office of Basic Energy Sciences, Office of Science, U.S. Department of Energy through Awards No. DE-SC0019484 (A.B. and S.M.C.) and KC030103172684 (N.G.) is gratefully acknowledged. S.M.C. gratefully acknowledges support from the Alexander von Humboldt foundation through the Feodor Lynen program. A portion of the computational work was performed using EMSL, a DOE Office of Science User Facility sponsored by the Office of Biological and Environmental Research and located at the Pacific Northwest National Laboratory (PNNL). PNNL is operated by Battelle Memorial Institute for the United States Department of Energy under DOE contract DE-AC05-76RL1830.

■ REFERENCES

- (1) Sansone, G.; Poletto, L.; Nisoli, M. High-energy attosecond light sources. *Nat. Photonics* **2011**, *5*, 655–663.
- (2) Popmintchev, T.; Chen, M.-C.; Popmintchev, D.; Arpin, P.; Brown, S.; Ališauskas, S.; Andriukaitis, G.; Balčiunas, T.; Mücke, O. D.; Pugzlys, A.; Baltuška, A.; Shim, B.; Schrauth, S. E.; Gaeta, A.; Hernández-García, C.; Plaja, L.; Becker, A.; Jaron-Becker, A.; Murnane, M. M.; Kapteyn, H. C. Bright Coherent Ultrahigh Harmonics in the keV X-ray Regime from Mid-Infrared Femtosecond Lasers. *Science* **2012**, *336*, 1287–1291.
- (3) Johnson, A. S.; Avni, T.; Larsen, E. W.; Austin, D. R.; Marangos, J. P. Attosecond soft X-ray high harmonic generation. *Philos. Trans. R. Soc., A* **2019**, *377*, 20170468.
- (4) Emma, P.; Akre, R.; Arthur, J.; Bionta, R.; Bostedt, C.; Bozek, J.; Brachmann, A.; Bucksbaum, P.; Coffee, R.; Decker, F.-J.; Ding, Y.; Dowell, D.; Edstrom, S.; Fisher, A.; Frisch, J.; Gilevich, S.; Hastings, J.; Hays, G.; Hering, P.; Huang, Z.; Iverson, R.; Loos, H.;

Messerschmidt, M.; Miahnahri, A.; Moeller, S.; Nuhn, H.-D.; Pile, G.; Ratner, D.; Rzepiela, J.; Schultz, D.; Smith, T.; Stefan, P.; Tompkins, H.; Turner, J.; Welch, J.; White, W.; Wu, J.; Yocky, G.; Galayda, J. First lasing and operation of an ångstrom-wavelength free-electron laser. *Nat. Photonics* **2010**, *4*, 641–647.

(5) Ishikawa, T.; Aoyagi, H.; Asaka, T.; Asano, Y.; Azumi, N.; Bizen, T.; Ego, H.; Fukami, K.; Fukui, T.; Furukawa, Y.; Goto, S.; Hanaki, H.; Hara, T.; Hasegawa, T.; Hatsui, T.; Higashiya, A.; Hirono, T.; Hosoda, N.; Ishii, M.; Inagaki, T.; Inubushi, Y.; Itoga, T.; Joti, Y.; Kago, M.; Kameshima, T.; Kimura, H.; Kirihara, Y.; Kiyomichi, A.; Kobayashi, T.; Kondo, C.; Kudo, T.; Maesaka, H.; Maréchal, X. M.; Masuda, T.; Matsubara, S.; Matsumoto, T.; Matsushita, T.; Matsui, S.; Nagasono, M.; Nariyama, N.; Ohashi, H.; Ohata, T.; Ohshima, T.; Ono, S.; Otake, Y.; Saji, C.; Sakurai, T.; Sato, T.; Sawada, K.; Seike, T.; Shirasawa, K.; Sugimoto, T.; Suzuki, S.; Takahashi, S.; Takebe, H.; Takeshita, K.; Tamasaku, K.; Tanaka, H.; Tanaka, R.; Tanaka, T.; Togashi, T.; Togawa, K.; Tokuhisa, A.; Tomizawa, H.; Tono, K.; Wu, S.; Yabashi, M.; Yamaga, M.; Yamashita, A.; Yanagida, K.; Zhang, C.; Shintake, T.; Kitamura, H.; Kumagai, N. A compact X-ray free-electron laser emitting in the sub-ångström region. *Nat. Photonics* **2012**, *6*, 540–544.

(6) Altarelli, M. The European X-ray free-electron laser facility in Hamburg. *Nucl. Instrum. Methods Phys. Res., Sect. B* **2011**, *269*, 2845–2849.

(7) Pellegrini, C.; Marinelli, A.; Reiche, S. The physics of x-ray free-electron lasers. *Rev. Mod. Phys.* **2016**, *88*, 015006.

(8) Bostedt, C.; Boutet, S.; Fritz, D. M.; Huang, Z.; Lee, H. J.; Lemke, H. T.; Robert, A.; Schlotter, W. F.; Turner, J. J.; Williams, G. J. Linac Coherent Light Source: The first five years. *Rev. Mod. Phys.* **2016**, *88*, 015007.

(9) Mukamel, S. *Principles of nonlinear optical spectroscopy*; Oxford University Press: Oxford, 1995.

(10) Mukamel, S.; Bakker, H. J. Preface: Special Topic on Multidimensional Spectroscopy. *J. Chem. Phys.* **2015**, *142*, 212101.

(11) Mukamel, S.; Healton, D.; Zhang, Y.; Biggs, J. D. Multidimensional attosecond resonant X-ray spectroscopy of molecules: Lessons from the optical regime. *Annu. Rev. Phys. Chem.* **2013**, *64*, 101–127.

(12) Bennett, K.; Zhang, Y.; Kowalewski, M.; Hua, W.; Mukamel, S. Multidimensional resonant nonlinear spectroscopy with coherent broadband x-ray pulses. *Phys. Scr.* **2016**, *T169*, 014002.

(13) Shen, Y. R. Surface properties probed by second-harmonic and sum-frequency generation. *Nature* **1989**, *337*, 519–525.

(14) Freund, I.; Levine, B. F. Optically Modulated X-Ray Diffraction. *Phys. Rev. Lett.* **1970**, *25*, 1241–1245.

(15) Eisenberger, P.; McCall, S. L. X-Ray Parametric Conversion. *Phys. Rev. Lett.* **1971**, *26*, 684–688.

(16) Glover, T. E.; Fritz, D. M.; Cammarata, M.; Allison, T. K.; Coh, S.; Feldkamp, J. M.; Lemke, H.; Zhu, D.; Feng, Y.; Coffee, R. N.; Fuchs, M.; Ghimire, S.; Chen, J.; Shwartz, S.; Reis, D. A.; Harris, S. E.; Hastings, J. B. X-ray and optical wave mixing. *Nature* **2012**, *488*, 603–608.

(17) Rouxel, J. R.; Kowalewski, M.; Bennett, K.; Mukamel, S. X-Ray Sum Frequency Diffraction for Direct Imaging of Ultrafast Electron Dynamics. *Phys. Rev. Lett.* **2018**, *120*, 243902.

(18) Rouxel, J. R.; Kowalewski, M.; Mukamel, S. Diffraction-Detected Sum Frequency Generation: Novel Ultrafast X-ray Probe of Molecular Dynamics. *J. Phys. Chem. Lett.* **2018**, *9*, 3392–3396.

(19) Cho, D.; Rouxel, J. R.; Kowalewski, M.; Lee, J.; Mukamel, S. Imaging of transition charge densities involving carbon core excitations by all X-ray sum-frequency generation. *Philos. Trans. R. Soc., A* **2019**, *377*, 20170470.

(20) Bennett, K.; Biggs, J. D.; Zhang, Y.; Dorfman, K. E.; Mukamel, S. Time-, frequency-, and wavevector-resolved x-ray diffraction from single molecules. *J. Chem. Phys.* **2014**, *140*, 204311.

(21) Tanaka, S.; Chernyak, V.; Mukamel, S. Time-resolved x-ray spectroscopies: Nonlinear response functions and Liouville-space pathways. *Phys. Rev. A: At., Mol., Opt. Phys.* **2001**, *63*, 063405.

- (22) Popova-Gorelova, D.; Santra, R. Imaging instantaneous electron flow with ultrafast resonant x-ray scattering. *Phys. Rev. B: Condens. Matter Mater. Phys.* **2015**, *91*, 184303.
- (23) Popova-Gorelova, D.; Santra, R. Imaging interatomic electron current in crystals with ultrafast resonant x-ray scattering. *Phys. Rev. B: Condens. Matter Mater. Phys.* **2015**, *92*, 184304.
- (24) Runge, E.; Gross, E. K. U. Density-Functional Theory for Time-Dependent Systems. *Phys. Rev. Lett.* **1984**, *52*, 997–1000.
- (25) Petersilka, M.; Gossmann, U.; Gross, E. Excitation energies from time-dependent density-functional theory. *Phys. Rev. Lett.* **1996**, *76*, 1212–1215.
- (26) Casida, M. E. *Recent Advances In Density Functional Methods: (Part I)*; World Scientific, 1995; pp 155–192.
- (27) Marques, M. A.; Gross, E. K. Time-Dependent Density Functional Theory. *Annu. Rev. Phys. Chem.* **2004**, *55*, 427–455.
- (28) Casida, M. E.; Huix-Rotllant, M. Progress in Time-Dependent Density-Functional Theory. *Annu. Rev. Phys. Chem.* **2012**, *63*, 287–323.
- (29) Bruner, A.; Hernandez, S.; Mauger, F.; Abanador, P. M.; LaMaster, D. J.; Gaarde, M. B.; Schafer, K. J.; Lopata, K. Attosecond Charge Migration with TDDFT: Accurate Dynamics from a Well-Defined Initial State. *J. Phys. Chem. Lett.* **2017**, *8*, 3991–3996.
- (30) Lopata, K.; Govind, N. Near and above ionization electronic excitations with non-hermitian real-time time-dependent density functional theory. *J. Chem. Theory Comput.* **2013**, *9*, 4939–4946.
- (31) Tong, X.-M.; Chu, S.-I. Time-Dependent Density-Functional Theory for Strong-Field Multiphoton Processes: Application to the Study of the Role of Dynamical Electron Correlation in Multiple High-Order Harmonic Generation. *Phys. Rev. A: At., Mol., Opt. Phys.* **1998**, *57*, 452–461.
- (32) Lein, M.; Kümmel, S. Exact Time-Dependent Exchange-Correlation Potentials for Strong-Field Electron Dynamics. *Phys. Rev. Lett.* **2005**, *94*, 143003.
- (33) Sissay, A.; Abanador, P.; Mauger, F.; Gaarde, M.; Schafer, K. J.; Lopata, K. Angle-Dependent Strong-Field Molecular Ionization Rates with Tuned Range-Separated Time-Dependent Density Functional Theory. *J. Chem. Phys.* **2016**, *145*, 094105.
- (34) Sándor, P.; Sissay, A.; Mauger, F.; Abanador, P. M.; Gorman, T. T.; Scarborough, T. D.; Gaarde, M. B.; Lopata, K.; Schafer, K. J.; Jones, R. R. Angle dependence of strong-field single and double ionization of carbonyl sulfide. *Phys. Rev. A: At., Mol., Opt. Phys.* **2018**, *98*, 043425.
- (35) Cho, D.; Rouxel, J. R.; Kowalewski, M.; Lee, J. Y.; Mukamel, S. Attosecond X-ray diffraction triggered by core or valence ionization of a dipeptide. *J. Chem. Theory Comput.* **2018**, *14*, 329–338.
- (36) Dreuw, A.; Weisman, J. L.; Head-Gordon, M. Long-Range Charge-Transfer Excited States in Time-Dependent Density Functional Theory Require Non-Local Exchange. *J. Chem. Phys.* **2003**, *119*, 2943–2946.
- (37) Stein, T.; Kronik, L.; Baer, R. Reliable Prediction of Charge Transfer Excitations in Molecular Complexes Using Time-Dependent Density Functional Theory. *J. Am. Chem. Soc.* **2009**, *131*, 2818–2820.
- (38) Petrone, A.; Lingerfelt, D. B.; Rega, N.; Li, X. From charge-transfer to a charge-separated state: a perspective from the real-time TDDFT excitonic dynamics. *Phys. Chem. Chem. Phys.* **2014**, *16*, 24457–24465.
- (39) Peng, B.; Lingerfelt, D. B.; Ding, F.; Aikens, C. M.; Li, X. Real-time TDDFT studies of exciton decay and transfer in silver nanowire arrays. *J. Phys. Chem. C* **2015**, *119*, 6421–6427.
- (40) Lopata, K.; Reslan, R.; Kowalska, M.; Neuhauser, D.; Govind, N.; Kowalski, K. Excited-state studies of polyacenes: a comparative picture using EOMCCSD, CR-EOMCCSD (T), range-separated (LR/RT)-TDDFT, TD-PM3, and TD-ZINDO. *J. Chem. Theory Comput.* **2011**, *7*, 3686–3693.
- (41) Tussupbayev, S.; Govind, N.; Lopata, K.; Cramer, C. J. Comparison of real-time and linear-response time-dependent density functional theories for molecular chromophores ranging from sparse to high densities of states. *J. Chem. Theory Comput.* **2015**, *11*, 1102–1109.
- (42) Glaesemann, K. R.; Govind, N.; Krishnamoorthy, S.; Kowalski, K. EOMCC, MRPT, and TDDFT studies of charge transfer processes in mixed-valence compounds: Application to the Spiro molecule. *J. Phys. Chem. A* **2010**, *114*, 8764–8771.
- (43) Jensen, L.; Govind, N. Excited states of DNA base pairs using long-range corrected time-dependent density functional theory. *J. Phys. Chem. A* **2009**, *113*, 9761–9765.
- (44) Govind, N.; Valiev, M.; Jensen, L.; Kowalski, K. Excitation energies of zinc porphyrin in aqueous solution using long-range corrected time-dependent density functional theory. *J. Phys. Chem. A* **2009**, *113*, 6041–6043.
- (45) Fischer, S. A.; Cramer, C. J.; Govind, N. Excited State Absorption from Real-Time Time-Dependent Density Functional Theory. *J. Chem. Theory Comput.* **2015**, *11*, 4294–4303.
- (46) Fischer, S. A.; Cramer, C. J.; Govind, N. Excited-state absorption from real-time time-dependent density functional theory: optical limiting in Zinc phthalocyanine. *J. Phys. Chem. Lett.* **2016**, *7*, 1387–1391.
- (47) Bowman, D. N.; Asher, J. C.; Fischer, S. A.; Cramer, C. J.; Govind, N. Excited-state absorption in tetrapyrrolyl porphyrins: comparing real-time and quadratic-response time-dependent density functional theory. *Phys. Chem. Phys.* **2017**, *19*, 27452–27462.
- (48) Srebro, M.; Govind, N.; De Jong, W. A.; Autschbach, J. Optical rotation calculated with time-dependent density functional theory: the OR45 benchmark. *J. Phys. Chem. A* **2011**, *115*, 10930–10949.
- (49) Lopata, K.; Van Kuiken, B. E.; Khalil, M.; Govind, N. Linear-response and real-time time-dependent density functional theory studies of core-level near-edge x-ray absorption. *J. Chem. Theory Comput.* **2012**, *8*, 3284–3292.
- (50) Fernando, R. G.; Balhoff, M. C.; Lopata, K. X-ray Absorption in Insulators with Non-Hermitian Real-Time Time-Dependent Density Functional Theory. *J. Chem. Theory Comput.* **2015**, *11*, 646–654.
- (51) Bruner, A.; LaMaster, D.; Lopata, K. Accelerated broadband spectra using transition dipole decomposition and Padé approximants. *J. Chem. Theory Comput.* **2016**, *12*, 3741–3750.
- (52) Liang, W.; Fischer, S. A.; Frisch, M. J.; Li, X. Energy-Specific Linear Response TDHF/TDDFT for Calculating High-Energy Excited States. *J. Chem. Theory Comput.* **2011**, *7*, 3540–3547.
- (53) Baczewski, A. D.; Shulenburger, L.; Desjarlais, M. P.; Hansen, S. B.; Magyar, R. J. X-ray Thomson Scattering in Warm Dense Matter without the Chihara Decomposition. *Phys. Rev. Lett.* **2016**, *116*, 115004.
- (54) Maitra, N. T.; Burke, K.; Woodward, C. Memory in time-dependent density functional theory. *Phys. Rev. Lett.* **2002**, *89*, 023002.
- (55) Maitra, N. T.; Zhang, F.; Cave, R. J.; Burke, K. Double excitations within time-dependent density functional theory linear response. *J. Chem. Phys.* **2004**, *120*, 5932–5937.
- (56) Cave, R. J.; Zhang, F.; Maitra, N. T.; Burke, K. A dressed TDDFT treatment of the 21Ag states of butadiene and hexatriene. *Chem. Phys. Lett.* **2004**, *389*, 39–42.
- (57) Nguyen, T. S.; Koh, J. H.; Lefelhocz, S.; Parkhill, J. Black-Box, Real-Time Simulations of Transient Absorption Spectroscopy. *J. Phys. Chem. Lett.* **2016**, *7*, 1590–1595.
- (58) Becke, A. D. A new mixing of Hartree–Fock and local density-functional theories. *J. Chem. Phys.* **1993**, *98*, 1372–1377.
- (59) Stephens, P.; Devlin, F.; Chabalowski, C.; Frisch, M. J. Ab initio calculation of vibrational absorption and circular dichroism spectra using density functional force fields. *J. Phys. Chem.* **1994**, *98*, 11623–11627.
- (60) Dunning, T. H., Jr Gaussian Basis Sets for Use in Correlated Molecular Calculations. I. The Atoms Boron Through Neon and Hydrogen. *J. Chem. Phys.* **1989**, *90*, 1007–1023.
- (61) Frisch, M. J.; Pople, J. A.; Binkley, J. S. Self-consistent molecular orbital methods 25. Supplementary functions for Gaussian basis sets. *J. Chem. Phys.* **1984**, *80*, 3265–3269.
- (62) Lopata, K.; Govind, N. Modeling Fast Electron Dynamics with Real-Time Time-Dependent Density Functional Theory: Application

to Small Molecules and Chromophores. *J. Chem. Theory Comput.* **2011**, *7*, 1344–1355.

(63) Valiev, M.; Bylaska, E.J.; Govind, N.; Kowalski, K.; Straatsma, T.P.; Van Dam, H.J.J.; Wang, D.; Nieplocha, J.; Apra, E.; Windus, T.L.; de Jong, W.A. NWChem: A Comprehensive and Scalable Open-Source Solution for Large Scale Molecular Simulations. *Comput. Phys. Commun.* **2010**, *181*, 1477–1489.

(64) Tretiak, S.; Mukamel, S. Density matrix analysis and simulation of electronic excitations in conjugated and aggregated molecules. *Chem. Rev.* **2002**, *102*, 3171–3212.

(65) Repisky, M.; Konecny, L.; Kadek, M.; Komorovsky, S.; Malkin, O. L.; Malkin, V. G.; Ruud, K. Excitation energies from real-time propagation of the four-component Dirac–Kohn–Sham equation. *J. Chem. Theory Comput.* **2015**, *11*, 980–991.

(66) Kadek, M.; Konecny, L.; Gao, B.; Repisky, M.; Ruud, K. X-ray absorption resonances near L 2, 3-edges from real-time propagation of the Dirac–Kohn–Sham density matrix. *Phys. Chem. Chem. Phys.* **2015**, *17*, 22566–22570.

(67) Ghosh, S.; Asher, J. C.; Gagliardi, L.; Cramer, C. J.; Govind, N. A semiempirical effective Hamiltonian based approach for analyzing excited state wave functions and computing excited state absorption spectra using real-time dynamics. *J. Chem. Phys.* **2019**, *150*, 104103.